Heliyon 10 (2024) e33568

Contents lists available at ScienceDirect

Heliyon

journal homepage: www.cell.com/heliyon

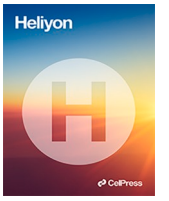

Research article

Synthesis and Modification of Boron Nitride nanotubes using ion implantation

L.I. Lisema [a,b,c,*], M. Madhuku [c], R. Erasmus [a,b], A. Shnier [b,d], D. Wamwangi [a,b], D.G. Billing [d], T.E. Derry [a,b]

[a] School of Physics, University of the Witwatersrand, Private Bag 3, Johannesburg, 2050, South Africa
[b] DST-NRF Centre of Excellence in Strong Materials (CoE-SM), University of the Witwatersrand, Private Bag 3, Johannesburg, 2050, South Africa
[c] iThemba LABS TAMS, Private Bag 11, Johannesburg, 2050, South Africa
[d] School of Chemistry, University of Witwatersrand, Private Bag 3, Johannesburg, 2050, South Africa

ARTICLE INFO

Keywords:
Chemical vapour deposition (CVD)
Boron nitride (BN)
Boron nitride nanotubes (BNNTs)
ion implantation

ABSTRACT

In this work, Chemical Vapour Deposition (CVD) has been used to synthesize boron nitride (BN) nanostructures, particularly nanotubes, and selectively introduce defects into the lattice of the synthesized BN nanostructures through ion implantation. Scanning electron microscopy (SEM) images show clear evidence of BN nanostructures and BN nanotubes (BNNTs), with the latter appearing as long, thin structures with diameters ranging from ~30–80 nm. Raman analysis show an E_{2g} mode of vibration assigned to hexagonal BN (h-BN) at 1366 cm^{-1} after ion implantation, with increased intensity. Grazing incidence X-ray diffraction (GIXRD) spectra revealed a prominent peak between 54 and 56°, corresponding to the (004) h-BN reflection, which was used to determine the average lattice parameter $c \sim 0.662$ nm representing the stacking direction of the BN layers. The majority of the samples had broad peaks, indicative of a nanocrystalline material. The only exception was the sample grown at 1200 °C, which was found to have a Scherrer crystallite size >100 nm. In contrast, the rest of the samples had an average size of 3.5 nm. Notable observations in this study include a significant rise in the size of the Raman derived crystallite domains in the nanostructures synthesized at 1100 and 1200 °C after ion implantation with boron ions at fluence 5×10^{14} ions/cm^2.

1. Introduction

Boron nitride nanotubes (BNNTs) have exceptional mechanical properties, with similar atomic bonding motifs to carbon with an effectively isoelectronic valency and being stable in a hexagonal structure of layered 2D sheets like graphite. Carbon nanotubes (CNTs) have been the focus of both experimental and theoretical research since their discovery in 1991 [1]. The methods that have been successful in creating carbon nanotubes (CNTs), such as arc discharge [2], ball-milling [3], laser ablation [4], substitution reaction of boron nitride (BN) atoms from CNT templates [5], and chemical vapour deposition [6], have also been used to produce boron nitride nanotubes (BNNTs). Each method involved specific precursors and conditions that were carefully chosen to facilitate the synthesis of BNNTs.

Unlike CNTs, which can be conductors or semiconductors depending on their chirality or helicity, BNNTs are always wideband gap

* Corresponding author. School of Physics, University of the Witwatersrand, Private Bag 3, Johannesburg, 2050, South Africa.
E-mail address: lehlohonolo.lisema@wits.ac.za (L.I. Lisema).

https://doi.org/10.1016/j.heliyon.2024.e33568
Received 4 October 2023; Received in revised form 20 June 2024; Accepted 24 June 2024
Available online 25 June 2024

semiconductors [7,8]. However, recent studies have unveiled novel applications for BNNTs, including osmotic power generation, room-temperature single-electron transistors, and high-brightness fluorophores [9]. Graphite and hexagonal boron nitride (h-BN) are similar parental structures to carbon nanotubes and boron nitride nanotubes, respectively. Both have hexagonal lattice layers, with h-BN is made up of alternating boron and nitrogen atoms, while graphite has carbon atoms in all positions. Hexagonal-BN exhibits a hexagonal close-packed (HCP) structure characterized by a two-layer stacking sequence (ABABA …), where adjacent layers consist of boron atoms positioned directly above nitrogen atoms. These layers form flat basal planes composed of B_3N_3 hexagonal rings, wherein each boron atom forms a bond with a nitrogen atom [10–12]. This unique layering arrangement is a significant characteristic of hexagonal-BN, with implications for its structural and functional properties. In graphite, the hexagons are misaligned and have variations in their stacking sequence. The in-plane lattice constants and interlayer distances of graphite and h-BN are $a_g = 0.246$ nm, $c_g/2 = 0.335$ nm, and $a_{BN} = 0.250$ nm, $c_{BN}/2 = 0.333$ nm, respectively, these values indicate that the interlayer distances in both graphite and h-BN are relatively large compared to the in-plane lattice constants, which suggests weak interlayer interactions. In both cases, the interlayer coupling is predominantly due to van der Waals forces [13,14].

Comparing the band structure of a single layer of boron nitride (BN) to a graphene sheet at the Fermi level reveals that they have distinctly different electronic properties (Fig. 1). In a graphite sheet, two bands intersect at the Fermi energy level at the K point, whereas in a single layer of h-BN, the non-overlap of these electronic states result in the formation of a forbidden band of energy 4.5 eV. CNTs can be either metallic or semiconductor in nature. All BNNTs, however, are semiconductors. BNNTs have a constant electron band gap of 5.5 eV regardless of tube diameter or chirality [15].

Selected properties of BNNTs and CNTs are compared in Table 1. These two materials have similar mechanical properties. However, BNNTs are more suitable for numerous electro-mechanical applications compared to their CNTs counterparts. Additionally, BNNTs, exhibit higher oxidation resistance and thermal stability in air compared to CNTs, enabling them to endure more extreme conditions and reactions. Their lower thermal conductivity enables them to be suitable for thermoelectric applications. BNNTs possess properties that are just as desirable for practical applications, if not more so, than carbon nanotubes [14]. As a result, there is great merit in furthering research on BNNTs.

In our previous work [19,20], we conducted experiments into the effects of ion implantation on bulk hexagonal BN (h-BN). As a result, we observed a transformation from h-BN to cubic-BN (c-BN) occurring in the subsurface region that was affected by the ion implantation process [21]. We successfully identified and established the parameters that govern this transformation. In this work, our focus is studying the effects of ion implantation on BNNTs using the same set of parameters, we aim to gain a better understanding of the transformation mechanism and its implications for BNNTs.

2. Experimental methods

2.1. Sample preparation

A silicon wafer (100) was cut into small ($\sim 10 \times 30$mm) pieces and placed in an ethanol-containing beaker. The Si-substrates were cleaned in an ultrasonic bath. The crucible was filled with a combination of boron (B), magnesium oxide (MgO), and iron (ii) oxide (Fe_2O_3) (2:1:1 M ratio), and the Si-substrates were put on top of the precursors,Fig. 2.

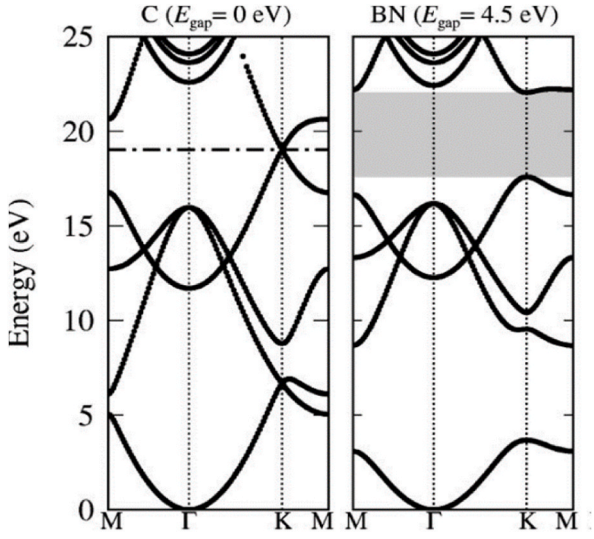

Fig. 1. The LDA (local density-functional approximation) band structure of BN sheet compared with that of a single graphite sheet in the hexagonal Brillouin zone. The Fermi level and band gap are indicated, respectively, by the dot-dashed line and the shaded area [15].

Table 1
The comparison of properties of BNNTS and CNTs.

	BNNTs	CNTs
Electrical properties [14]	Always semiconducting [above 4 eV gap]	Metallic or semiconducting
Mechanical properties [Young's modulus] [16]	1.18 TPa	1.33 TPa
Thermal conductivity [14]	600 W/mK	3000 W/mK
Oxidation resistance [17]	Stable up to 800 °C	Stable up to 300–400 °C in air
Elastic Modulus [18]	~850 GPa	150 GPa

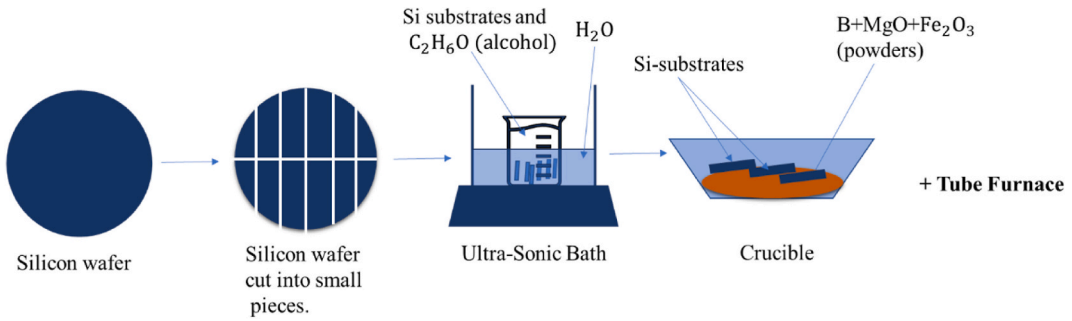

Fig. 2. Flow diagram, illustrating the preparation of samples.

2.2. Chemical vapour deposition (CVD)

The crucible containing the precursors and Si substrates was placed in a quartz tube inside the tube furnace, after sealing both ends, argon gas (Ar) was fed through the system to eliminate air and produce an inert atmosphere at room temperature. Simultaneously, the temperature was gradually raised at a rate of 10 °C/min up to the desired process temperature. At this temperature, the argon gas flow was halted, and ammonia (NH_3) gas fed into the system at ~ 200 sccm for the production of BNNTs. The CVD syntheses were carried out for 1 h at 900, 1000, 1100 and 1200 °C, Fig. 3 [6].

At high temperatures, B_xO_y vapours will react with NH_3 to generate BNNTs. MgO and Fe_2O_3 operate as catalysts for this process [22]. Water is effective in the filtration system for the removal of ammonia vapour by the formation of ammonium hydroxide.

2.3. Ion implantation

The ion implantations were performed at iThemba LABS in South Africa, using the Varian-Extrion 200-20A2F ion implanter. All implantations were done using B^+ ions at room temperature at energy 150 keV and Fluences of 1×10^{14} and 5×10^{14} ions/cm^2 as in Aradi et al. [20] and our prior work [21].

2.4. Scanning electron microscopy

The measurements were conducted using a ZEISS Sigma 300 VP Scanning Electron Microscope, which is located in the School of Mechanical, Industrial, and Aeronautical Engineering at the University of the Witwatersrand. The electron beam energy was adjusted

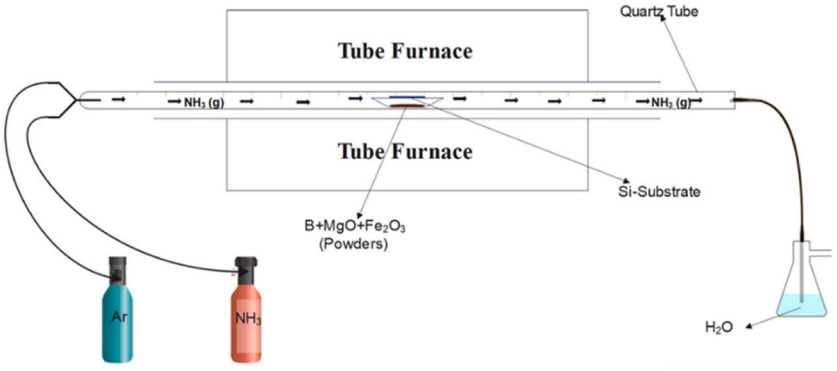

Fig. 3. A diagram illustrating the CVD synthesis procedure.

in the range of 3 kV–15 kV, depending on the specific samples being analyzed.

2.5. Raman characterization

Raman spectroscopy measurements of the samples were taken before and after ion implantation using the 514.5 nm line of an argon ion laser and an Olympus BX40 microscope attached to a Horiba LabRAM HR Raman spectrometer. The incident beam was focused onto the sample using a 100× objective (N.A. = 0.90) and the backscattered light was dispersed via a 600 lines/mm grating onto a liquid nitrogen cooled CCD detector. The data was acquired using LabSpec v5 software. The incident beam power was kept low (<0.4 mW at the sample) to prevent localised heating. The laser beam diameter at the sample was ~ 1 μm. Multiple spots were measured on each sample and representative spectra are plotted in the Results section.

2.6. Grazing incidence XRD

GIXRD measurements were conducted on the samples both prior to and after ion implantation using the D8 discover ADVANCE Bruker X-ray Diffractometer, which is located in the School of Chemistry at the University of the Witwatersrand. The diffractometer is outfitted with CuKα radiation with a wavelength of λ = 1.5406 Å and is operated at a voltage of 40 kV with a current of 40 mA.

3. Results and discussion

3.1. Stopping and range of ions in matter (SRIM)

Fig. 4 shows the SRIM simulations on the distribution of the number of vacancies per ion and unit length (Å) in h-BN, caused by the implantation of boron ions (B^+) at 150 keV. Notably, the curve shows that for boron ions at energy 150 keV, the range of ion penetration depth is approximately 0.4 μm. To calculate the damage density or vacancy concentration $\boldsymbol{C(x)}$ in the material, one needs to multiply the mean number of vacancies ($\boldsymbol{C_p}$) generated by the damage distribution for each ion per unit length by the fluence ($\boldsymbol{D}$) over the total area, Equation (1). At 150 keV, the probability of nuclear stopping is expected to be low due to the relatively low atomic number of boron thus the stopping will be mostly electronic.

$$\boldsymbol{C}(\boldsymbol{x}) = \boldsymbol{C_p} \times \boldsymbol{D} \quad (1)$$

Therefore, at energy 150 keV at room temperature, at fluences of 1×10^{14} and 5×10^{14} ions/cm^2 we get the vacancy concentration for boron implantation as given in Table 2.

3.2. Scanning electron microscopy (SEM)

3.2.1. Samples prepared at 900 °C

Fig. 5 shows Boron Nitride cauliflower-like structures of the sample synthesized at 900 °C for a growth duration of 1 h, prior to ion implantation.

3.2.2. Samples prepared at 1000 °C

Fig. 6 shows the SEM image of BN nanostructures synthesized at 1000 °C prior to ion implantation. It is clear from the image that

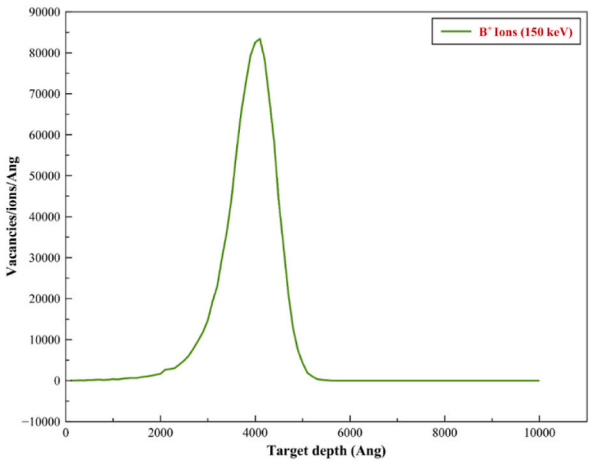

Fig. 4. The graph generated by the SRIM model shows the relationship between the depth of penetration and the number of vacancies per ion and unit length (measured in Å) for boron ions at 150 keV.

Table 2
The determined concentration of damage density in the material.

Ions	Optimum fluence (10^{14}ions/cm^2)	C_p (vacancies/10^{-8}cm-ion)	R_p (Å)	C(x) (10^{21}vac/cm^3)
Boron	1	2.75×10^{-2}	3.7×10^3	0.28
	5	2.75×10^{-2}	3.7×10^3	1.4

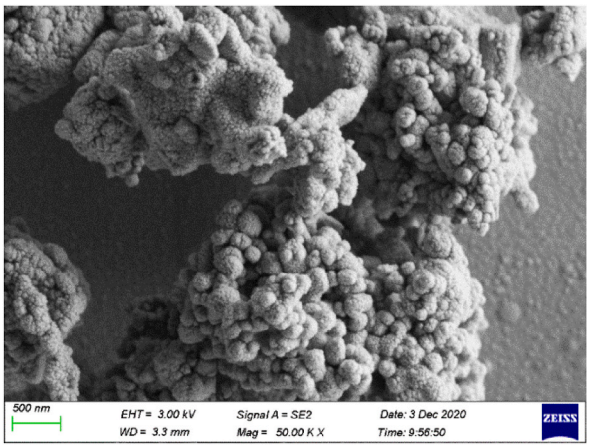

Fig. 5. SEM image of synthesized Boron Nitride cauliflower-like nanocomposites at 900 °C.

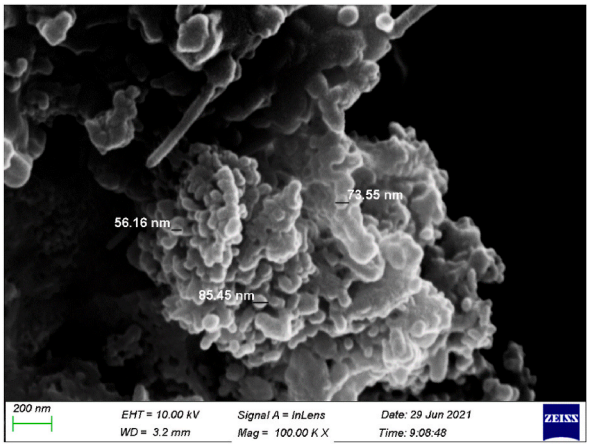

Fig. 6. SEM micrograph of synthesized Boron Nitride nanocomposites at 1000 °C with the diameter of selected particles/composites/features indicated.

raising the temperature has an impact on how the BN nanocomposites behave; there are some nanotubes (50–80 nm diameter) and a cauliflower-like nanostructure.

3.2.3. Samples prepared at 1100 °C

The BNNTs synthesized at 1100 °C prior to ion implantation are depicted in a SEM image in Fig. 7. The tubes (~40–80 nm diameter) show swollen tip characteristics that are found on many nanotubes.

3.2.4. Samples prepared at 1200 °C

The SEM images of samples synthesized at 1200 °C in Fig. 8 (prior to implantation) show the presence of BN nanostructures at various magnifications. It is clear that various shapes of BN nanostructures were synthesized, cauliflower-like composites, nanospheres, and poly-dispersed nanotubes (~30–40 nm) can be observed. Most of the latter have strong curvatures.

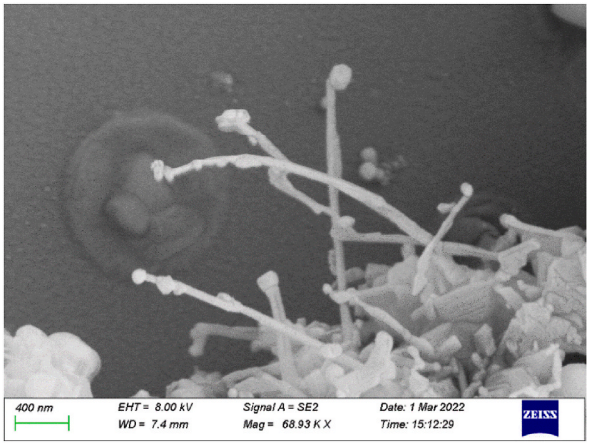

Fig. 7. SEM image of boron nitride nanotubes (BNNTs) synthesized at 1100 °C.

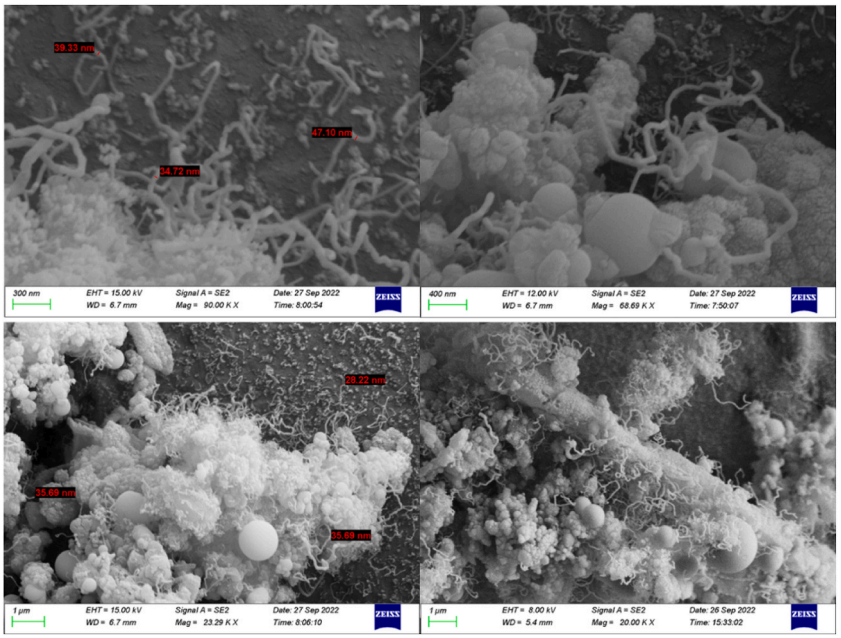

Fig. 8. SEM images of sample synthesized at 1200 °C, showing BN nanostructures of different shapes at different magnification, including many nanotubes. The diameters of representative nanotubes are indicated in red. (For interpretation of the references to colour in this figure legend, the reader is referred to the Web version of this article.)

3.3. Growth mechanism of boron nitride nanostructures

The formation of boron nitride nanostructures, especially nanotubes (Figs. 7 and 8) using the chemical vapour deposition method, can be explained by the theory of nucleation [6,22]. The probability of nucleation is given by

$$P_N = Be^{-\left(\frac{\pi\sigma^2}{k^2T^2\ ln\ \alpha_s}\right)} \quad (2)$$

The equation involves several variables, including B (a constant), σ (surface energy), and α_s (the supersaturation ratio, calculated as p/p_o). p is the vapour pressure of the growth species, p_0 is the equilibrium vapour pressure of the condensed phase, k is the Boltzman constant and T is the absolute temperature in Kelvin.

From Equation (2), P_N is proportional to $\exp\left(-\frac{1}{T^2}\right)$. This indicates that an increase in temperature increases the probability of nanotube nucleation. This is evident from the growth of nanotubes when the experimental temperature was increased from 900 °C to

1200 °C in increments of 100 °C. Secondly, the surface energy of the metal oxide catalyst also affects the probability of nucleation for nanostructures. MgO and Fe_2O_3 were used in this work. Supersaturation $\boldsymbol{\alpha_s}$ and $\boldsymbol{P_N}$ are also proportional meaning if the partial pressure of the growth species rises, the level of supersaturation will increase. Consequently, there will be a greater probability of nucleation of BN nanostructures due to the heightened degree of supersaturation caused by the increased partial pressure of the growth species. This was accomplished by layering Si-substrates on top of the precursors in a crucible enclosed within a sealed quartz tube in an NH_3-filled atmosphere. The CVD experimental setup is intended to collect and capture growth species in order to improve the nucleation rate of BN nanostructures formed by reacting with NH_3 gas.

This means that when BNNTs are synthesized using boron (B), magnesium oxide (MgO), and iron oxide (FeO) as precursors. The production of BNNTs follows the Vapour Liquid Solid (VLS) growth process, Tang et al. [23] and Zhi et al. [24], because at a certain temperature, the interaction of the compounds produces B_2O_2 vapours (i.e., melted catalyst particles) [25]. These catalysts condensate on the substrate when their partial vapour pressures are suitably raised. The produced B_2O_2 vapour combines with N_2 from the NH_3 gas to form the BN-species. These species are subsequently diffused into the condensed catalysts until they precipitate as BNNTs [26].

3.3.1. Synthesized BNNTs morphology

From the SEM images BN nanostructures and BN nanotubes can be observed. BNNTs appear as long, thin structures with relatively uniform diameters, while the nanostructures appear as irregularly shaped structures clustered together forming cauliflower-like shapes with varying sizes. Fig. 8, which is the SEM image of samples prepared at a temperature of 1200 °C; shows BN-nanospheres of different sizes and BNNTs dispersed throughout the surface of the sample.

3.3.2. Synthesized BNNTs diameters

BNNTs in the SEM images have diameters of ~30–80 nm, which is consistent with the reported diameters in previous studies [27]. The diameter of BNNTs can affect the mechanical, electrical, or other properties of the BNNTs [28]. In a study conducted by Chen et al. [29], examining the mechanical properties of individual BNNTs, the findings demonstrated that the effective transverse elastic modulus of the BNNTs increases with the number of tube walls and decreases with an increase in diameter. The diameter of the BNNTs can also affect their electrical properties, such as their electrical conductivity and bandgap. Smaller diameter BNNTs have been shown to have wider bandgaps and lower electrical conductivity than larger diameter BNNTs [30]. Therefore, the ~30–80 nm diameter range of the BNNTs in the SEM image suggest that they have relatively wide bandgaps and low electrical conductivity, which could limit their use in electronic applications that require high conductivity and smaller bandgap.

The diameter of the BNNTs can also affect other properties, such as their thermal conductivity and effective surface area for electrochemical applications. Smaller diameter BNNTs have been shown to have higher thermal conductivity and surface area than larger diameter BNNTs [28,30]. Therefore, the 30–80 nm diameter range of the BNNTs in the SEM image suggest that they have relatively high thermal conductivity and surface area, which could make them suitable for applications that require efficient heat transfer or high surface area, such as catalyst support.

At an energy of 150 keV, the range of a boron ion in BNNTs can be estimated to be about ~400 nm using the SRIM software package. This means that the boron ions are expected to pass through several BNNTs in the size range of 30–80 nm before coming to a stop. This suggests that the primary mechanism for energy loss of the boron ions in BNNTs will be through electronic stopping. The contribution of nuclear stopping to the total energy loss of the boron ions is expected to be small at this energy.

3.4. Raman characterization

The penetration depth of a particular wavelength of light into a material is defined as the depth at which the intensity (or power) of the electric field of the light has decayed to a value that corresponds to a fraction of 1/e of the incident light. Using this definition, laser penetration depth ($\boldsymbol{P}$), is calculated by taking the inverse of the absorption coefficient ($\boldsymbol{\alpha}$), that is $\boldsymbol{P} = \boldsymbol{\alpha}^{-1}$.

The absorption coefficient is calculated by using,

$$\boldsymbol{\alpha} = \frac{\boldsymbol{4\pi k_e}}{\boldsymbol{\lambda}} \tag{3}$$

where $\boldsymbol{k_e}$ is the extinction coefficient (0.041 for *h*-BN) and λ is the photon's wavelength. For a 514.5 nm laser (2.41 eV) and an h-BN sample, $\boldsymbol{P}$ is calculated to be approximately 1 μm. According to SRIM simulations in Fig. 4, the range of implantation for boron at 150 keV is approximately 0.4 μm. During the Raman spectroscopy measurements, the laser penetrates significantly deeper than the ion implantation range, thus ensuring that all potential implantation damage is sampled during the measurement.

It is anticipated that the typical optical vibration phonon modes of h-BN with space group $P6_3/mmc$ will be present at the Brillouin zone centre [31], represented by the following equation

$$\boldsymbol{\Gamma} = \boldsymbol{2B_{lg}} + \boldsymbol{A_{2u}} + \boldsymbol{E_{lu}} + \boldsymbol{2E_{2g}} \tag{4}$$

Equation (4) represents the optically inactive phonon mode, which is denoted as $\boldsymbol{2B_{lg}}$, and is not observed in any optical vibrational spectrum. The in-plane B–N bending and out-of-plane B–N stretching of boron nitride, which correspond to $\boldsymbol{A_{2u}}$ and $\boldsymbol{E_{lu}}$, respectively, and are infrared-active phonon vibrational modes, are not expected to be present in the visible Raman spectrum. The final component of the equation represents the Raman active mode ($\boldsymbol{E_{2g}}$), which typically exhibits two vibrational centres. These symmetry centres are produced by the displacement of both boron and nitrogen atoms in both the in-plane and out-of-plane directions [32].

Hexagonal BN has one intense Raman peak (E_{2g} mode) at 1366 cm^{-1}. It is the typical B–N bond stretching vibration within the basal planes and it depicts the high frequency vibrational Raman mode [33]. The second Raman peak at 51.8 cm^{-1} is associated with the layer shearing vibration between the basal layers and is a low frequency mode [31,33].

Before ion implantation, samples synthesized at 1000 °C did not show any peak in the vicinity of 1366 cm^{-1} (Fig. 9), while sample synthesized at 1100 °C and 1200 °C showed a clear broad peak in the range 1350–1370 cm^{-1} (Figs. 10 and 11). This is attributed to the presence of amorphous h-BN in these samples.

After ion implantation, the Raman spectra of samples implanted with ion fluence 5×10^{14} ions/cm^2 at 1000 °C (Fig. 9) show an amorphous *h-BN* peak, and a narrower, more intense E_{2g} vibrational mode of h-BN is observed around 1366 cm^{-1} for samples synthesized at 1100 °C and 1200 °C (Figs. 10 and 11). Raman analysis did not show any E_{2g} mode of vibration of *h-BN* for all samples at fluence 1×10^{14} ions/cm^2. The samples synthesized at 900 °C had no active 1366 cm^{-1} Raman peak present.

The peaks have shifted towards lower wavenumbers by range of 1–8 cm^{-1} Figs. 9 and 10, the downshift of these peaks from the 1366 cm^{-1} E_{2g} h-BN mode could be linked to a nanoscale crystal of h-BN possibly produced. This can be explained using the phonon confinement mode by Parayanthal and Pollak [34]. Thus, this red shift is due to the induced strain during ion implantation and this effect dominates in bilayer, causing shifts of the Raman peak to lower wavenumbers. The FHWM of the E_{2g} vibrational mode for Raman spectra of samples implanted with ion fluence 5×10^{14} ions/cm^2 at 1100 and 1200 °C varies from 9 to 12 cm^{-1} and is comparable to the one found in R. V. Gorbachev et al. for monolayers [35].

The effects of ion implantation can be explored by determining the average crystallite domain size. The work done by Nemanich et al. [36] is relevant, as they used the same excitation wavelength as in this work. They showed that the average crystallite domain size ($\boldsymbol{L}$) can be determined by the following equation (Fig. 7 of ref [36]):

$$\boldsymbol{FWHM} = \frac{\mathbf{1417}}{\boldsymbol{L}} + \mathbf{8.7} \tag{5}$$

where $\boldsymbol{L}$ is the average crystallite domain size (in Å) and $\boldsymbol{FWHM}$ is the h-BN Raman peak FWHM in cm^{-1} units.

Table 3 below has the calculated average crystallite domain size values. The width of a Raman peak is related to phonon lifetime, and this is governed by the average crystallite domain size. The phonon will have a short lifetime for small domain size, meaning the FWHM is large, and for a large domain size the phonon will have a longer lifetime, meaning FWHM is smaller. Fig. 12 displays the average crystallite domain size as a function of FWHM of the Raman E_{2g} mode of vibration of h-BN. An increase in domain size is observed after ion implantation, because ions are neutral at the end of their range (low ionization state). After coming to rest, the ion takes up electrons (e.g., from the conduction band) and gets back to its normal neutral state, i.e., becomes an atom. A narrow FWHM is associated with a more crystalline material, i.e., increased crystallinity and either the absence of inhomogeneous strain or very little such strain is present. These findings imply that ion implantation promotes or improves the growth of BN nanostructures with sp^2 hybridized planar bonding.

The key finding in this study is the significant enhancement of crystallite domain size (i.e., an increase in $\boldsymbol{L}$) in samples synthesized at 1100 °C after boron ion implantation at a fluence of 5×10^{14} ions/cm^2. The effect can also be observed in samples grown at 1200 °C but reduced. These conditions may be optimal for promoting growth of the BN crystallites. The increase in crystallite domain size after ion implantation with boron ions can also be attributed to the presence of boron atoms in the lattice [37].

3.5. Grazing incidence XRD characterization

The collected GIXRD patterns, both before and after ion implantation present a peak near 55.4° 2θ. This peak is consistent across the data-set, additional features are observed at lower angles, yet these are poorly defined above the background noise and are only observed for subsets of the patterns, Figs. 13–16. The data was compared to the literature structures COD 9008834 and COD 9008997 of cubic and hexagonal BN, respectively, from the Crystallography Open Database [38]. The cubic structure offered no peaks comparable to the collected data, while the (004) peak from the hexagonal phase (h-BN) is consistent with the ~55.4° 2θ peak. This peak cannot be attributed to the Si substrate, nor Si_3N_4, SiB_x, MgO (101), or Fe_xO_y (440) phases which were considered due to the components used during synthesis [39,40].

The absence of the full set of expected peaks could potentially be justified by a preferred crystallite growth orientation. In context of the (002) peak expected near ~26.7° 2θ, the scattering vector being probed by the GIXRD would be ~84° with respect to the surface, for the (004) peak this is ~77°, in combination with a preferred orientation, this difference can potentially explain the absence of the (002) peak. The possibility of preferred crystallite orientation cannot be taken for granted and thus warrants further investigation. Additionally, the formation of unidentified phases cannot be ruled out, this provides sufficient information to consider h-BN or a closely related structure as a possible source of the observed GIXRD peaks.

3.5.1. Refined structural details

The ~54° 2θ peak was tentatively assigned to the (004) h-BN peak index. From this, the sample crystallinity can be considered using peak width as a proxy. This can be interpreted using the Scherrer crystallite size which is related to size of the coherent scattering domains in the structure. The presented values consider broadening from a 3 mm X-ray beam footprint and no additional instrument broadening factors making them a lower bound estimate. When considering nanomaterials, the sample broadening dominates the overall peak broadening making estimates for such materials a reasonable approximation even without a comprehensive instrument profile description. The majority of samples provided broad peaks indicative of a nano-crystalline material with the exception of the

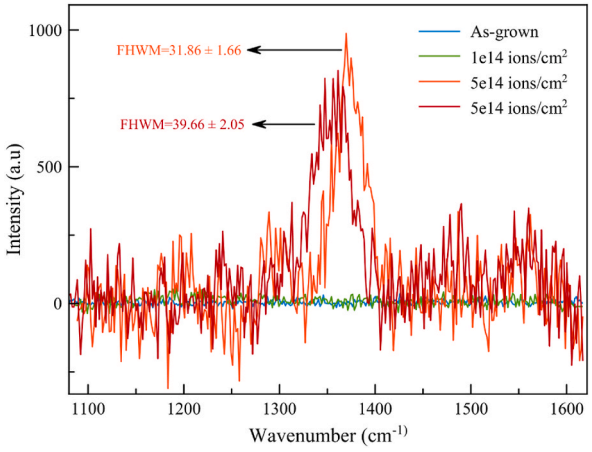

Fig. 9. Raman Spectra of CVD prepared h-BN nanostructures at 1000 °C.

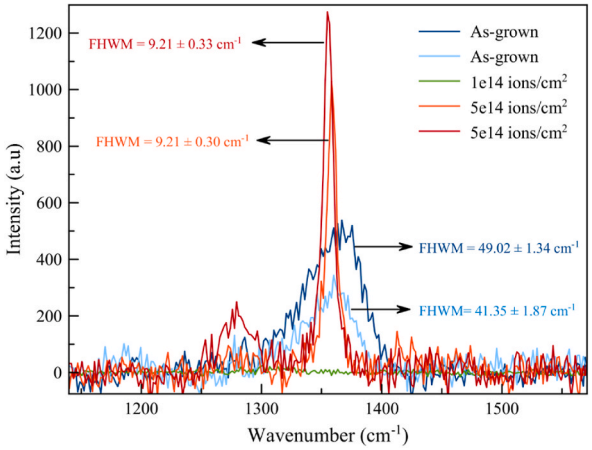

Fig. 10. Raman Spectra of CVD prepared BNNTs at 1100 °C.

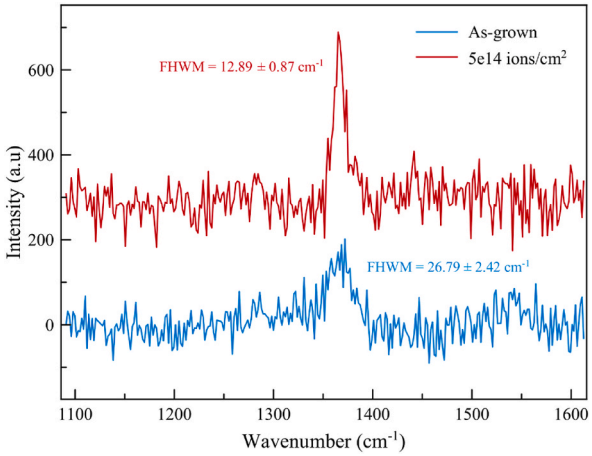

Fig. 11. Raman Spectra of BN nanostructures prepared at 1200 °C.

Table 3
Raman derived calculated Average crystallite domain size.

	As-grown		5×10^{14} ions/cm^2	
T (°C)	FWHM (cm^{-1})	Average crystallite domain size (nm)	FWHM (cm^{-1})	Average crystallite domain size (nm)
900	–	–	–	–
1000	–	–	31.9 ± 2	6.1 ± 0.3
	–	–	39.7 ± 2	4.6 ± 0.2
1100	49 ± 1.3	3.5 ± 0.1	9.2 ± 0.3	270 ± 10
	41.4 ± 1.9	4.3 ± 0.2	9.2 ± 0.3	280 ± 9.1
1200	26.8 ± 2.2	7.8 ± 0.7	12.9 ± 0.9	34.0 ± 2.3

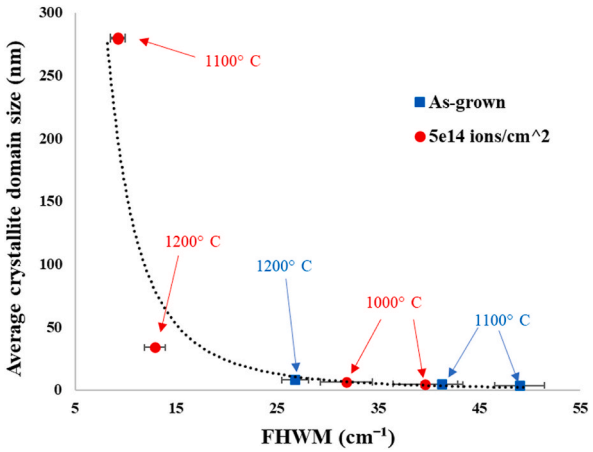

Fig. 12. Graph of the Raman peak derived average crystallite domain size as a function of FWHM.

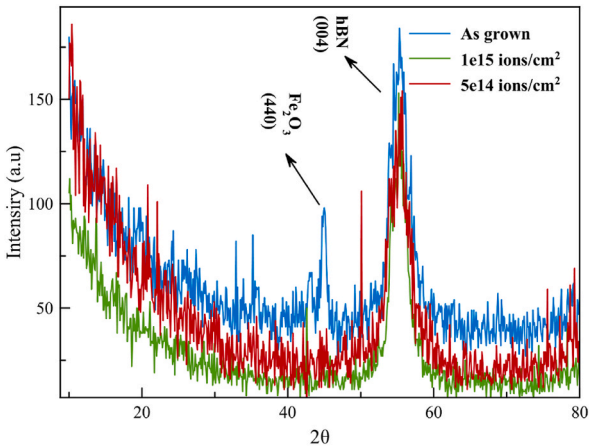

Fig. 13. Grazing incidence XRD spectra of h-BN cauliflower-like nanocomposites grown at 900 °C.

1200 °C as-grown sample. The latter was refined to a ~115 nm crystallite size with the balance of samples represented by an average size of 3.5 nm ($\sigma = 0.3$ nm). The difference between these values is suggested to be a result of the formation of alternative structural features as observed in the SEM microscopy. At 1200 °C nano-spheres with sizes as large as a few hundred nanometres are formed which could explain the narrower diffraction peak. This is not observed in the XRD patterns after ion implantation, which is a process with the potential to segment scattering domains. This is converse to the Raman measurements in which there is an increased coherent interaction volume on implantation.

The c-axis lattice parameter was refined using the position of the tentatively assigned (004) h-BN peak. The values below 1200 °C were sufficiently close with no clear trends, such that they are described by the average of 0.662 nm ($\sigma = 0.0006$ nm). For the 1200 °C samples the c-axis showed relative tensile strain with implantation with lattice parameters of 0.658, 0.662, and 0.663 nm for the as-deposited, 1×10^{14} and 5×10^{14} ions/cm^2 samples respectively.

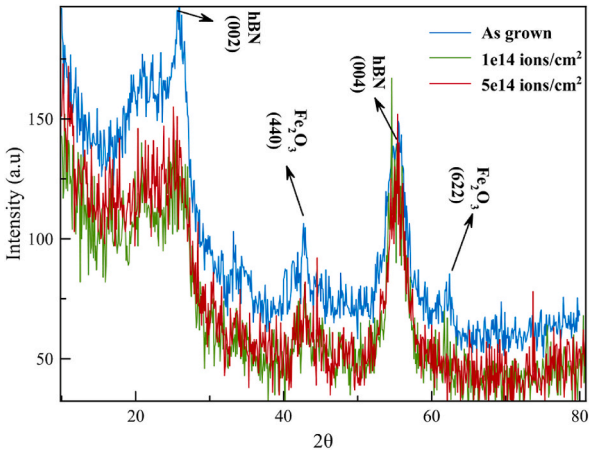

Fig. 14. Grazing XRD spectra of h-BN nanostructures grown at 1000 °C.

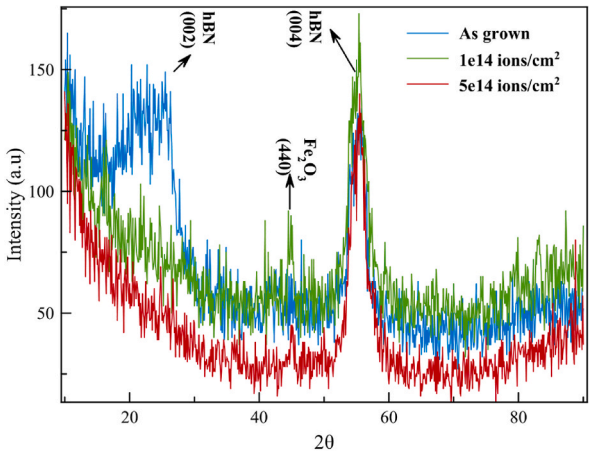

Fig. 15. Grazing incidence XRD Spectra of BN nanotubes grown at 1100 °C.

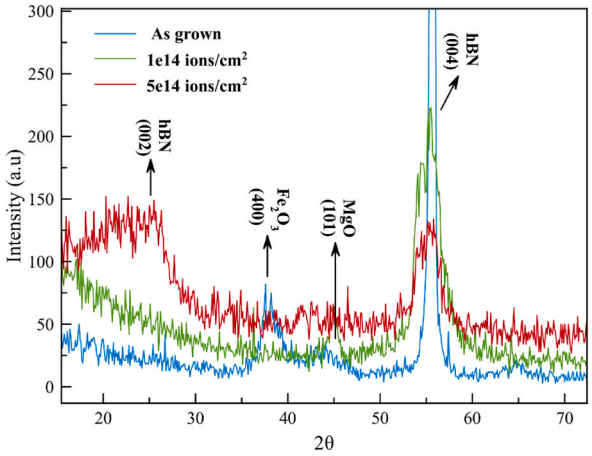

Fig. 16. GIXRD spectra of CVD samples prepared at 1200 °C.

Similarly, the differences in integrated intensity for samples prepared below 1200 °C was 32.8 ($\sigma = 7.2$) where variations in substrate size between samples could account for the intensity variations. This was not the case for the 1200 °C samples where a marked decreasing trend in intensity was observed with ion implantation with values of 122, 41, and 27 for the as-grown, 1×10^{14} and 5×10^{14} ions/cm^2 samples, respectively.

4. Summary

BN nanostructures and BNNTs were evident in the SEM images of samples prepared at 1000 °C, 1100 °C and 1200 °C. In contrast to the nanostructures which appeared clumped together to create cauliflower-like shapes with various sizes, BNNTs were long, thin structures with almost identical diameters.

Prior to ion implantation, samples synthesized at 1000 °C showed no peak in the vicinity of 1366 cm^{-1}, whereas samples synthesized at 1100 °C and 1200 °C displayed a definite broad peak in the range 1350–1370 cm^{-1}. This is due to the existence of amorphous h-BN in these samples.

The Raman spectra of samples implanted with ion fluence 5×10^{14} ions/cm^2 at 1000 °C exhibit an amorphous h-BN peak, while samples produced at 1100 °C and 1200 °C had more intense E_{2g} vibrational mode of h-BN about 1366 cm^{-1}. For all samples, Raman analysis revealed no E_{2g} mode of vibration of h-BN at fluence 1×10^{14} ions/cm^2. There was no active 1366 cm^{-1} Raman signal in the samples synthesized at 900 °C.

The effects of ion implantation were also explored by determining the Raman derived average crystallite domain size. The most notable outcome of the experiment was the significant enhancement in the crystallite domain size of the 1100 °C samples after ion implantation with boron ions at a fluence of 5×10^{14} ions/cm^2. The effect is also observed in the 1200 °C samples but to a lesser extent.

XRD analysis revealed a well-defined 55.4° 2θ peak consistent with a h-BN (004) peak.

When using Raman spectroscopy, we need to be mindful of where we take measurements. The laser beam used in Raman spectroscopy is very small, about 1 μm wide. So, we can only measure tiny clusters of material on the silicon substrate at a time. It's not possible to measure all the groups individually. On the other hand, with grazing X-ray diffraction (GXRD), the beam is much wider, allowing us to get a better average of the structures on the surface.

5. Conclusion

Synthesis of BNNTs was successful at 1100 °C and 1200 °C CVD temperature. The BNNTs were long, thin structures with diameters around ~30–80 nm range, whereas the nanostructures appeared as amorphous structures clumped together to create cauliflower-like shapes with various sizes. The Raman analysis detected a peak at 1367 cm^{-1}, which indicates the presence of sp^2 hybridized BN planar bonding and was attributed to the high frequency E_{2g} mode for the h-BN peak. This peak was more distinctly observed at 1100 and 1200 °C, both before and after ion implantation. The Raman derived average crystallite domain size values confirmed that after ion implantation the phonon lifetime was longer because of the large domain size, this means that the BN nanostructures are more crystallized. The increase in Raman derived crystallite domain size of BN nanostructures after ion implantation with boron ions can be attributed to a number of factors. During ion implantation, energetic ions are implanted into the material, causing damage and creating vacancies in the crystal lattice. As a result, the implanted material undergoes a process of annealing and recrystallization as the vacancies are gradually filled in by atoms diffusing through the lattice. This process can lead to an increase in the size of the crystallite domains, which are regions of the material where the atoms are in a crystal lattice.

CRediT authorship contribution statement

L.I. Lisema: Writing – review & editing, Writing – original draft, Resources, Methodology, Investigation, Formal analysis. **M. Madhuku:** Writing – review & editing, Supervision. **R. Erasmus:** Writing – review & editing. **A. Shnier:** Writing – review & editing. **D. Wamwangi:** Writing – review & editing. **D.G. Billing:** Supervision. **T.E. Derry:** Writing – review & editing, Supervision.

Declaration of competing interest

The authors declare that they have no known competing financial interests or personal relationships that could have appeared to influence the work reported in this paper.

Acknowledgements

The financial assistance of DST-NRF Centre of Excellence in Strong Materials (CoE-SM) towards this research is hereby acknowledged.

Opinions expressed and conclusions arrived at are those of the author and are not necessarily to be attributed to the CoE-SM.

References

[1] S. Iijima, Helical microtubules of graphitic carbon, Nature 354 (6348) (1991) 56–58.

[2] Y.W. Yeh, Y. Raitses, B.E. Koel, N. Yao, Stable synthesis of few-layered boron nitride nanotubes by anodic arc discharge, Sci. Rep. 7 (1) (2017) 1–7, https://doi.org/10.1038/s41598-017-03438-w.

[3] Y. Chen, J.F. Gerald, J.S. Williams, S. Bulcock, Synthesis of boron nitride nanotubes at low temperatures using reactive ball milling, Chem. Phys. Lett. 299 (3–4) (1999) 260–264, https://doi.org/10.1016/S0009-2614(98)01252-4.

[4] D. Golberg, Y. Bando, M. Eremets, K. Takemura, K. Kurashima, H. Yusa, Nanotubes in boron nitride laser heated at high pressure, Appl. Phys. Lett. 69 (14) (1996) 2045–2047, https://doi.org/10.1063/1.116874.

[5] Y. Chen, L.T. Chadderton, J.F. Gerald, J.S. Williams, A solid-state process for formation of boron nitride nanotubes, Appl. Phys. Lett. 74 (20) (1999) 2960–2962, https://doi.org/10.1063/1.123979.

[6] C.H. Lee, J. Wang, V.K. Kayatsha, J.Y. Huang, Y.K. Yap, Effective growth of boron nitride nanotubes by thermal chemical vapor deposition, Nanotechnology 19 (45) (2008), https://doi.org/10.1088/0957-4484/19/45/455605.

[7] Y. Huang, et al., Thin boron nitride nanotubes with exceptionally high strength and toughness, Nanoscale 5 (11) (2013) 4840–4846, https://doi.org/10.1039/c3nr00651d.

[8] A. Maguer, E. Leroy, L. Bresson, E. Doris, A. Loiseau, C. Mioskowski, A versatile strategy for the functionalization of boron nitride nanotubes, J. Mater. Chem. 19 (9) (2009) 1271–1275, https://doi.org/10.1039/b815954h.

[9] D. Zhang, et al., Emerging applications of boron nitride nanotubes in energy harvesting, electronics, and biomedicine, ACS Omega 6 (32) (2021) 20722–20728, https://doi.org/10.1021/acsomega.1c02586.

[10] Y. Shi, et al., Synthesis of few-layer hexagonal boron nitride thin film by chemical vapor deposition, Nano Lett. 10 (10) (2010) 4134–4139, https://doi.org/10.1021/nl1023707.

[11] M.J. Molaei, M. Younas, M. Rezakazemi, A comprehensive review on recent advances in two-dimensional (2D) hexagonal boron nitride, ACS Appl. Electron. Mater. 3 (12) (2021) 5165–5187, https://doi.org/10.1021/acsaelm.1c00720.

[12] P.B. Mirkarimi, K.F. McCarty, D.L. Medlin, Review of advances in cubic boron nitride film synthesis, Mater. Sci. Eng. R Rep. 21 (2) (1997) 47–100, https://doi.org/10.1016/S0927-796X(97)00009-0.

[13] T.Q.P. Vuong, et al., Isotope engineering of van der Waals interactions in hexagonal boron nitride, Nat. Mater. 17 (2) (Feb. 2018) 152–158, https://doi.org/10.1038/nmat5048.

[14] M. Ishigami, "Properties of boron nitride nanotubes," in AIP Conf. Proc., vol. 94, no. 1, pp. 94–99, doi: 10.1063/1.1639682.

[15] Y.H. Kim, K.J. Chang, S.G. Louie, Electronic structure of radially deformed BN and BC3 nanotubes, Phys. Rev. B Condens. Matter 63 (20) (2001) 1–5, https://doi.org/10.1103/PhysRevB.63.205408.

[16] A. Zettl, N.G. Chopra, Measurement of the elastic modulus of a multi wall boron nitride nanotube, Solid State Commun. 105 (5) (1998) 297–300.

[17] Y. Chen, J. Zou, S.J. Campbell, G. Le Caer, Boron nitride nanotubes: pronounced resistance to oxidation, Appl. Phys. Lett. 84 (13) (2004) 2430–2432, https://doi.org/10.1063/1.1667278.

[18] X. Blase, A. Rubio, S.G. Louie, M.L. Cohen, Stability and band gap constancy of boron nitride nanotubes, Epl 28 (5) (1994) 335–340, https://doi.org/10.1209/0295-5075/28/5/007.

[19] E. Aradi, R.M. Erasmus, T.E. Derry, Formation of c-BN nanoparticles by helium, lithium and boron ion implantation, Nucl. Instruments Methods Phys. Res. Sect. B Beam Interact. with Mater. Atoms 272 (2012) 57–60, https://doi.org/10.1016/j.nimb.2011.01.032.

[20] E. Aradi, S.R. Naidoo, R.M. Erasmus, B. Julies, T.E. Derry, Investigations on the characterization of ion implanted hexagonal boron nitride, Nucl. Instruments Methods Phys. Res. Sect. B Beam Interact. with Mater. Atoms 307 (2013) 214–217, https://doi.org/10.1016/j.nimb.2012.12.118.

[21] T.E. Derry, L.I. Lisema, A.T. Magabe, E. Aradi, R. Machaka, M. Madhuku, Allotrope conversion and surface hardness increase in ion implanted boron nitride, Surf. Coating. Technol. 355 (2018) 61–64, https://doi.org/10.1016/j.surfcoat.2018.04.005.

[22] D. Köken, P. Sungur, H. Cebeci, F.Ç. Cebeci, Revealing the effect of sulfur compounds for low-temperature synthesis of boron nitride nanotubes from boron minerals, ACS Appl. Nano Mater. 5 (2) (2022) 2137–2146, https://doi.org/10.1021/acsanm.1c03858.

[23] C. Tang, Y. Bando, T. Sato, K. Kurashima, A novel precursor for synthesis of pure boron nitride nanotubes, Chem. Commun. 2 (12) (2002) 1290–1291, https://doi.org/10.1039/b202177c.

[24] C. Zhi, Y. Bando, C. Tan, D. Golberg, Effective precursor for high yield synthesis of pure BN nanotubes, Solid State Commun. 135 (1–2) (2005) 67–70, https://doi.org/10.1016/j.ssc.2005.03.062.

[25] R.S. Wagner, W.C. Ellis, Vapor-liquid-solid mechanism of single crystal growth, Appl. Phys. Lett. 4 (5) (1964) 89–90, https://doi.org/10.1063/1.1753975.

[26] A. Pakdel, C. Zhi, Y. Bando, T. Nakayama, D. Golberg, A comprehensive analysis of the CVD growth of boron nitride nanotubes, Nanotechnology 23 (21) (2012) 215601, https://doi.org/10.1088/0957-4484/23/21/215601.

[27] S. Kalay, Z. Yilmaz, O. Sen, M. Emanet, E. Kazanc, M. Çulha, Synthesis of boron nitride nanotubes and their applications, Beilstein J. Nanotechnol. 6 (1) (2015) 84–102, https://doi.org/10.3762/bjnano.6.9.

[28] X. Chen, C. Ke, Structural and physical properties of boron nitride nanotubes and their applications in nanocomposites, in: Boron Nitride Nanotubes in Nanomedicine, William Andrew Publishing, 2016, pp. 183–199.

[29] X. Chen, C.M. Dmuchowski, C. Park, C.C. Fay, C. Ke, Quantitative characterization of structural and mechanical properties of boron nitride nanotubes in high temperature environments, Sci. Rep. 7 (1) (2017) 1–9, https://doi.org/10.1038/s41598-017-11795-9.

[30] S.I. Kundalwal, V. Choyal, Enhancing the piezoelectric properties of boron nitride nanotubes through defect engineering, Phys. E Low-Dimensional Syst. Nanostructures 125 (June 2020) (2021) 114304, https://doi.org/10.1016/j.physe.2020.114304.

[31] R. Geich, C.H. Perry, G. Rupprecht, Normal modes in hexagonal boron nitride, Phys. Rev. B 146 (2) (1966) 543–547.

[32] R.J. Nemanich, S.A. Solin, R.M. Martin, Light scattering study of boron nitride microcrystals, Phys. Rev. B 23 (12) (1981) 6843, 6355.

[33] K. Nakamura, M. Fujitsuka, M. Kitajima, Disorder-induced line broadening in first-order Raman scattering from graphite, Phys. Rev. B 41 (1990) 12260–12263.

[34] P. Parayanthal, F. Pollak, Raman scattering in alloy semiconductors:" spatial correlation" model, Phys. Rev. Lett. 52 (20) (1984) 1822, https://doi.org/10.1103/PhysRevLett.52.1822.

[35] R.V. Gorbachev, et al., Hunting for monolayer boron nitride: optical and Raman signatures, FWP J 28 (5) (1988) 1–5.

[36] R.J. Nemanich, S.A. Solin, R.M. Martin, Light scattering study of boron nitride microcrystals, Phys. Rev. B 23 (12) (1981) 6348–6356, https://doi.org/10.1103/PhysRevB.23.6348.

[37] J.F. Prins, T.E. Derry, Radiation defects and their annealing behaviour in ion-implanted diamonds, Nucl. Instruments Methods Phys. Res. Sect. B Beam Interact. with Mater. Atoms 166 (2000) 364–373, https://doi.org/10.1016/S0168-583X(99)01190-8.

[38] S. Grażulis, D. Chateigner, R.T. Downs, A.F.T. Yokochi, M. Quirós, L. Lutterotti, Crystallography Open Database–an open-access collection of crystal structures, J. Appl. Crystallogr. 42 (4) (2009) 726–729.

[39] O. Karaagac, H. Kockar, A simple way to obtain high saturation magnetization for superparamagnetic iron oxide nanoparticles synthesized in air atmosphere: optimization by experimental design, J. Magn. Magn Mater. 409 (2016) 116–123, https://doi.org/10.1016/j.jmmm.2016.02.076.

[40] R.R. Gandhi, M. Sundararajan, J. Suresh, A comparative study on antibacterial properties of MgO nanoparticles prepared under different calcination temperature, Dig. J. Nanomater. Biostruct. 7 (3) (2012) 983–989.